



ELSEVIER

Available online at [www.sciencedirect.com](http://www.sciencedirect.com)

SCIENCE @ DIRECT®

Icarus ●●● (●●●●) ●●●-●●●

ICARUS

[www.elsevier.com/locate/icarus](http://www.elsevier.com/locate/icarus)

## A closer look at main belt asteroids 1: WF/PC images

A.D. Storrs<sup>a,\*</sup>, C. Dunne<sup>b</sup>, J.-M. Conan<sup>c</sup>, L. Mugnier<sup>c</sup>, B.P. Weiss<sup>d</sup>, B. Zellner<sup>e</sup><sup>a</sup> Department of Physics, Astronomy, and Geosciences, Towson University, 8000 York Road, Towson, MD 21252, USA<sup>b</sup> Towson H.S., Cedar Ave., Towson, MD 410-887-3608, USA<sup>c</sup> ONERA, Département d'Optique Théorique et Appliquée, BP 72, F-92322 Chatillon cedex, France<sup>d</sup> Department of Earth, Atmospheric, and Planetary Sciences, 54-724 Massachusetts Institute of Technology, Cambridge, MA 02139, USA<sup>e</sup> Department of Physics, GA Southern University, Landrum Box 8031, Statesboro, GA 30460, USA

Received 5 July 2002; revised 3 August 2004

### Abstract

We present new reconstructions of images of main belt Asteroids 9 Metis, 18 Melpomene, 19 Fortuna, 216 Kleopatra, and 624 Hektor, made with the uncorrected Wide-Field/Planetary Camera (WF/PC) on the Hubble Space Telescope (HST). Deconvolution with the MISTRAL algorithm demonstrates that these asteroids are clearly resolved. We determine diameters, albedos, and lower limits to axial ratios for these bodies. We also review the process used to restore the aberrated images. No surface features or companions are found, but the rotation of 216 Kleopatra is clearly seen. The asteroidal albedos are similar to those determined by other procedures.

© 2004 Elsevier Inc. All rights reserved.

*Keywords:* Main-belt asteroids; Image processing

### 1. Introduction

With the advent of diffraction-limited imaging in visible light available with Hubble Space Telescope (HST), the unresolved bodies orbiting between Mars and Jupiter are point sources no longer. While spacecraft flybys and rendezvous with individual asteroids have provided unprecedented detail on individual objects, at present our best tool for high spatial resolution observations of large numbers of main belt asteroids in the visible region remains HST. Adaptive optics imaging has made great strides recently (see review by [Close, 2000](#)) but is generally limited to the infrared where the increased aperture of the ground based telescopes is mostly offset by the increased wavelength of the photons. Furthermore, adaptive optics systems only correct over a small field of view, whereas HST imaging is diffraction limited over its whole field of view. Adaptive optics searches for asteroidal companions have been much more fruitful than

searches with HST ([Merline et al., 2001](#)) largely due to the much greater amount of telescope time available to them.

Two programs of HST observations imaged main belt asteroids before corrections for spherical aberration in the primary mirror were installed. These were described by [Storrs et al. \(1999\)](#), and focused on searching for companions to the asteroids. No companions were observed, despite the fact that previous studies of these bodies ([Hartmann, 1979](#)) had identified companions that should have been easily observable from HST. [Storrs et al. \(1999\)](#) noted that in addition to searching for companions, some of the primary asteroids were slightly extended in the images. Their image restoration with the Maximum Entropy (MEM) algorithm produced artifacts around the edges of these small objects, however, and they observed that "... no constraint on the surface heterogeneity can be made from this data."

Five of the ten asteroids imaged by these two programs (109 Felicitas, 146 Lucina, 434 Hungaria, 532 Herculina, and 674 Rachele) did not appear significantly extended in the reconstructions and so are not discussed here. These were discussed in [Storrs et al. \(1999\)](#).

\* Corresponding author. Fax: +410-704-3511.

E-mail address: [astorrs@towson.edu](mailto:astorrs@towson.edu) (A.D. Storrs).

In this paper we return to the resolved asteroids with a new image reconstruction algorithm. Reconstruction of extended planetary images tends to restore the sharp edges but the high spatial frequency associated with these edges will often cause the correction to overshoot on the bright side of the edge. This effect is often called “ringing.” We tuned the input parameters of the MISTRAL algorithm to avoid these “ringing” effects. We compare independent reductions of multiple observations of each asteroid. Where more than one filter is used, we look for color changes across the disk of the resolved asteroid. In all cases we compare the albedo, size, and shape to that reported in the literature (Table 3).

## 2. MISTRAL

We restored the images (largely removing the effects of spherical aberration) using the Myopic Iterative STep Preserving ALgorithm (MISTRAL) routine developed by a team at the Office National d’Etudes et de Recherches Aérospatiales (ONERA). A good description is contained in Conan et al. (1998) and in Mugnier et al. (2003), and the edge preserving prior in Conan et al. (2000). MISTRAL is “myopic” in that it can restore images with an incomplete knowledge of the PSF. It is called “myopic” rather than blind to stress the fact that the available information on the PSF, though partial, is used to constrain the deconvolution.

MISTRAL includes an edge preserving regularization process that eliminates the “ringing” effect induced in restorations of planetary images by standard algorithms (e.g., MEM or Lucy). These standard algorithms generally do well for fields of point sources or slowly varying continuous sources, but will overcorrect a sharp edge on an extended object, such as a planet’s sunlit limb. For small objects such as asteroids, this overcorrection can fill the entire “disk,” eliminating any information on brightness variegation on the asteroid.

MISTRAL’s edge-preserving process has two user parameters that must be varied to provide the best reconstruction of each image. These are called “regobj” (which controls the fidelity to the data and fidelity to the object prior) and “threshold” (which controls the balance between quadratic noise smoothing behavior and the linear edge preserving behavior—see Conan et al., 2000, for more detail). For each image, we ran a grid of reconstructions, first reducing regobj until “ringing” occurred, and then using the last “good” value of regobj and reducing threshold until the reconstruction became broken up. The smallest “good” values of regobj and threshold are used to restore the image, and these values are reported in Table 2. As the reconstructions were run in batch mode, the number of iterations was not always recorded, but varied between 100 and 1000. The smaller values were generally for restorations with smaller regobj and threshold. Figure 1 illustrates this process: regobj decreases from right to left, and threshold decreases from top to bot-

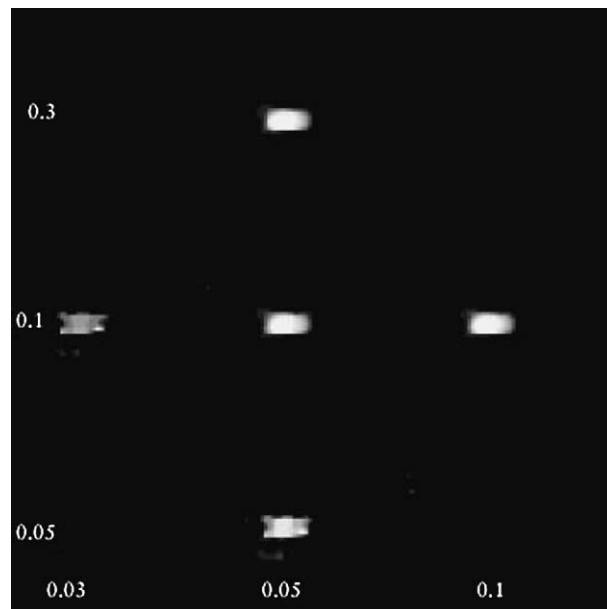


Fig. 1. Parameter optimization: reconstructions of the same image with the same PSF and decreasing “regobj” (0.1, 0.05, 0.03) from right to left, and decreasing “threshold” (0.3, 0.1, 0.05) from top to bottom. The reconstructions look similar until critical values of these parameters are reached. Bottom and left-most images are over-corrected.

tom. The appearance of the reconstruction does not vary greatly until the critical values are reached.

The noise model controls the likelihood term used in the deconvolution (Conan et al., 2000). The noise is initially modeled as spatially varying white (Gaussian) and then both the detector noise and photon noise are estimated from the image itself prior to the actual deconvolution.

Note that in this process we assumed that there really is no unusual brightening at the edge of the disk, and that the brightness varies smoothly across the disk. These are reasonable assumptions as the brightness variation for one of the best observed asteroids, 4 Vesta, is only about 10% (Zellner et al., 1997). Saint-Pé et al. (1993) also report a smooth Lambertian brightness variation across the disk of 1 Ceres in their AO observations.

The PSF for HST is very stable. It can be reproduced well by the software program “Tiny Tim” (Krist, 1993). Thus we used MISTRAL in its classical mode, where the PSF is not updated by the program. In fact, the PSF can be calculated to a higher spatial resolution than that observed (0.043 arcsec per pixel for the WF/PC). We made use of these oversampled PSFs and the high signal-to-noise ratio (SNR) of the asteroidal images to restore them at four times the spatial scale at which they were made. Thus in the restorations, each pixel subtends only 0.011 arcsec. The effect of this can clearly be seen in simulated data in Fig. 2, and in real data in Fig. 6, which shows before and after restorations of four images of asteroid 216 Kleopatra.

Note that at the time of the observations of 216 Kleopatra the line of sight was closely aligned with the asteroid’s rotational axis, and during the observations the asteroid is

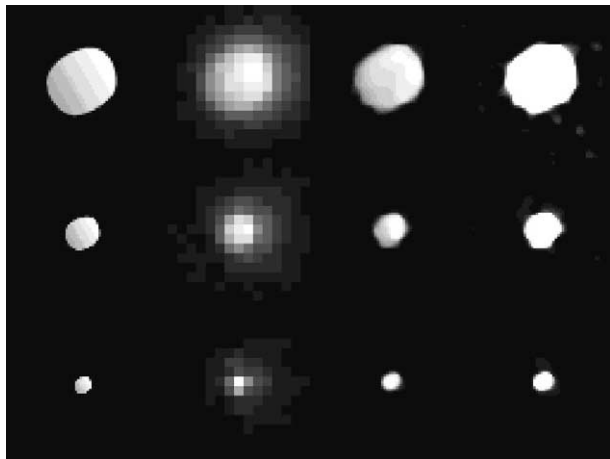


Fig. 2. Image reconstruction test. The left column are (noiseless) input images, the next column those same images after being convolved with a (noiseless) PSF, rebinning to WF/PC resolution, and adding (Gaussian) photon and read noise. The third column shows the results of deconvolution with MISTRAL—note the high fidelity to the input image, especially for the smallest case (bottom row). The right column is the restored image “cut” at the level that has the same area as the input image—generally 1/4 maximum rising to 1/2 maximum for the smallest image.

expected to rotate about  $20^\circ$ . Although some change is seen among the raw WF/PC images, it is difficult to discern anything systematic. The elongation of the asteroid and its rotation are clearly seen in the restorations, however. The data are not quite good enough to shed light on the question of whether 216 Kleopatra is a binary system, a contact binary, or very elongated—a 20 km gap between two larger objects of comparable brightness would be lost in this reconstruction process, given this observational circumstance. At the time of these observations, a single subpixel subtends 27 km, and a gap would have to be two subpixels wide to be unambiguously detected (see below).

The effects of MISTRAL restoration were modeled by convolving an image whose area is known, with a subsampled TinyTim PSF. This image is then reduced to WF/PC resolution, shot and read noise are added to match that of the WF/PC data (typically  $\text{SNR} = 60$ ), and the result restored with optimum MISTRAL parameters. Some results are shown in Fig. 2. The improvement to the (aberrated) WF/PC images is quite noticeable, especially for the smallest image (bottom row for Fig. 2).

The area of the restoration matched the area of the input image at 1/4 the maximum value for all but the smallest images. For restorations less than 150 subpixels area (about  $2.5 \times 4$  WF/PC pixels) the restoration area matched at slightly higher intensities. For example the areas matched at 0.4 times max for 100 subpixels area, and at 0.8 times max for 40 subpixels area. This is shown in the 4th column of Fig. 2, where the restored image is “cut” at a fraction of its peak value. The area of the restored image at the level of the cut equals the area of the input image. This effect does not depend on the filter used, and is reflected in the dimensions of each asteroid reported in Table 3. Only the areas of 216

Kleopatra and 624 Hektor were below 200 subpixels and so the dimensions were measured at a higher brightness level (0.3 times max to 0.5 times max, respectively) on the reconstructions.

The uncertainties in the linear dimensions are  $\pm 1$  subpixel, consistent with the spread in these measurements over multiple observations of each asteroid. These measurements were made at the same brightness level of the reconstructed image as the area measurement, and the right column of Fig. 2 shows the reconstructed model images displayed at that level. The uncertainty in the albedo is dominated by the uncertainty in the area measurement. The difference in area among successive observations of each asteroid was always less than 10 subpixels, so this value was used in determining the uncertainty in the albedo measurements reported in Table 3, which is a conservative value.

Note that Hestroffer et al. (2002b) report using MISTRAL on AO images of 216 Kleopatra, although they do not use this “super-resolution” technique. While they see two clearly separated bodies they do not supply any quantitative information on their size or the size of the gap between them.

The improvement in WF/PC images by this reconstruction technique is obvious in Fig. 2. Spherical aberration limits the Strehl ratio in an unrestored WF/PC F439W image to 5% (that is, peak flux observed is 5% of that expected for an unaberrated optical system). Note that for WFPC-2 images (corrected for the error in the HST primary mirror), the Strehl ratio is 27%. When a WF/PC standard star image is restored in the “super-resolution” mode used here, 59% of the flux is left in the central sixteen subpixels of the restored image (compared to 4% of the flux in the unrestored image). This corresponds to a Full Width at Half Maximum (FWHM) of 0.043 arcsec, while the FWHM of a WFPC-2 (unaberrated) PSF is typically 0.036 arcsec. Note that WFPC-2 images have about 37% of their flux in the peak after restoration, but only 19% before—MISTRAL restoration does not improve WFPC-2 (unaberrated) images as much as it does WF/PC (aberrated) images.

### 3. Data

The data are summarized in Table 1 (after Storrs et al., 1999). All observations of a given asteroid were made in one orbit of HST around the Earth. This constrains the viewing period to 45 min or so. In practice, the longest span of observations was  $< 20$  min for the faintest body, 624 Hektor, with observations of the brighter objects taking only 10 min or so.

The data were processed with the standard HST data pipeline, using the “best” calibration files and “High-Fidelity flats” (Biretta et al., 1995)<sup>1</sup> and other calibration files as recommended by the HST data archive. Photometric measure-

<sup>1</sup> Biretta, J., Ritchie, C., Baggett, S., Mackenty, J., 1995. WF/PC-1 FLAT FIELD CLOSURE CALIBRATION: <http://www.stsci.edu/ftp/>

Table 1  
Observational circumstances

Asteroid	Observed (1993)	$R$ (AU)	$\Delta$ (AU)	Phase ( $^{\circ}$ )	Program	Filter(s)	Exp. time (s)	App. mag.	Angular size (arcsec)
9 Metis	17 Aug. 01:29	2.321	1.485	17	4521	F555W	2.0	9.89	0.21
18 Melpomene	18 Jan. 09:20	2.220	1.255	9	4764	F439W	2.0	9.47	0.21
19 Fortuna	10 Sept. 12:44	2.301	1.534	20	4521	F555W	5.0	11.27	0.20
216 Kleopatra	2 July 15:33	3.243	2.384	11	4764	F439W, F555W	7.0	12.24, 12.29	0.13
624 Hektor	13 June 13:54	5.239	4.333	5	4764	F439W, F555W	100, 40	14.86, 14.79	0.11

ments were done in accordance with the HST Data Handbook ([http://www.stsci.edu/hst/HST\\_overview/documents/datahandbook](http://www.stsci.edu/hst/HST_overview/documents/datahandbook)) (in Europe, try the link from the mirror website, <http://www.stecf.org/hstdocs>). A multiplicative flux correction of  $3.68 \pm 0.02$  for the F439W “B” images and  $3.62 \pm 0.02$  for the F555W “V” images (flux was measured in the unrestored images in a box 0.69 arcsec square, the same size as the unrestored images in Figs. 3–7) was determined by measuring the encircled energy in images of the standard star BD + 75D325. These factors are the major source of error in the absolute photometry (and hence, in the determination of the albedo). Corrections were also applied to all images for instrumental contamination. Values of up to 15% for “B” images of 216 Kleopatra and 624 Hektor (which were taken almost a year after the last instrument decontamination) were found by interpolation of Fig. 46-10 of the Data Handbook.

The F555W filter approximates the Johnson V band. Its center is at 525.2 nm and FWHM is 122.3 nm. The F439W filter approximates the Johnson B band. Its center is at 429.2 nm and FWHM is 46.4 nm.

WF/PC observations of the white dwarf standard star BD + 75D325 were reduced with the same photometry routine give an F555W magnitude of 9.58, 0.04 magnitudes from the commonly used value of  $V = 9.54$ . The color of this star, measured in the same manner as the colors of the asteroids reported here, is  $-0.96$ . The flux ratio determined from the spectrum published by Collins and Bohlin (1997) is  $-0.90$ . Thus the photometry system used here results in a color that is more blue than expected by one standard deviation (that is, the error in the photometry multiplied by the square root of 2, since the errors in the F439W and F555W photometry are equal). The effect of this bias is discussed further in the sections pertaining to asteroids 216 Kleopatra and 624 Hektor.

For reconstruction, a small section ( $128 \times 128$  pixels,  $\sim 5.6$  arcsec square) centered on each asteroid was extracted from the pipeline processed image, and manually cleaned of cosmic ray hits. A Tiny Tim PSF was generated for the WF/PC camera for the time, filter, and location of the image. As mentioned above, this was generated at four times the ordinary spatial resolution. The data were then replicated

Table 2  
MISTRAL parameters

Asteroid	Filter	Exp. time (s)	Peak counts	Regobj	Threshold
9 Metis	F555W	0.4	746	0.3	0.1
9 Metis	F555W	1	1820	0.3	0.3
9 Metis	F555W	2	3887 <sup>a</sup>	0.5	0.3
18 Melpomene	F439W	0.5	199	0.1	0.1
18 Melpomene	F439W	0.5	205	0.1	0.1
18 Melpomene	F439W	2	813	0.3	0.3
18 Melpomene	F439W	2	821	0.3	0.3
19 Fortuna	F555W	2	1012	0.3	0.3
19 Fortuna	F555W	4	1970	0.3	0.3
19 Fortuna	F555W	10	3905 <sup>a</sup>	1.0	1.0
216 Kleopatra	F439W	7	315	0.03	0.1
216 Kleopatra	F439W	7	319	0.03	0.1
216 Kleopatra	F555W	3	803	0.05	0.1
216 Kleopatra	F555W	3	831	0.05	0.1
624 Hektor	F439W	100	434	0.03	0.03
624 Hektor	F439W	100	481	0.03	0.03
624 Hektor	F555W	40	1548	0.03	0.1
624 Hektor	F555W	40	1574	0.03	0.1

<sup>a</sup> Saturated image.

(using SINC interpolation) to the same resolution, so that each pixel of WF/PC data became 16 pixels. These were then processed using the MISTRAL parameters given in Table 2. Variation among image brightness and integration time, as well as the wavelengths at which the observations were made, account for the differences in the values used for the best restoration. Note that the size of the image that is restored has little effect on the restoration as long as the bulk of the energy in the image and in the PSF is contained in the area restored.

#### 4. Results

Figs. 3 through 7 show the unrestored and restored images of asteroids, 9 Metis, 18 Melpomene, 19 Fortuna, 216 Kleopatra, and 624 Hektor. For 216 and 624, two different filters were used and so Fig. 8 shows the ratio of the average of the restorations of the “B” (F439W) and “V” (F555W) images for these two objects. Table 3 summarizes the physical parameters derived from these images. Note that “PDSSBN” refers to NASA’s Planetary Data System Small Bodies Node, at URL <http://pdsbn.astro.umd.edu/sbnhtml/>.

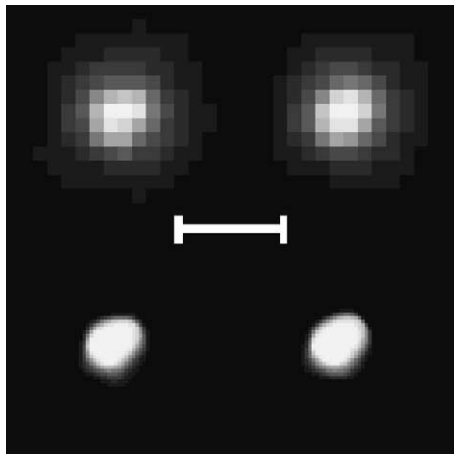


Fig. 3. Images of Asteroid 9 Metis before (top row) and after (bottom) reconstruction with the MISTRAL algorithm and a Tiny Tim PSF. Data taken on 17 August 1993 at 01:29 UT and 01:35 UT, in the F555W filter. The line of sight is nearly aligned with the rotational axis but little rotation may be seen (the asteroid should have rotated  $15^\circ$  during the 12 m duration of the exposure sequence). The scale bar is 0.37 arcsec long and celestial North is  $70^\circ$  CW from straight up. Note that the third image mentioned in Table 2 is saturated and is not included in the figure. Photometry was done on the area shown in this image (a box 0.69 arcsec square).

The rotation pole and period information are generally from lightcurve observations, and while there are often several solutions in the database, they are generally in agreement or 180 degrees apart. The “TRIAD” values in Table 3 are from the “Supplementary IRAS Minor Planet Survey” by Tedesco et al. (2002).

#### 4.1. 9 Metis

Figure 3 shows the processed and reconstructed unsaturated images of 9 Metis. The top row of images is the result of the standard “pipeline” processing, and the bottom row the results of MISTRAL reconstruction of these images. This is among the best resolved asteroid of this set, but no surface markings are visible. The bright regions on the limb reported by Storrs et al. (1999) using Maximum Entropy (MEM) reconstructions have disappeared with the new reconstruction algorithm.

The size is significantly larger than reported by Tedesco (1989) but only one sigma larger than that determined by radar observations (Ostro et al., 1985). The albedo is calculated to be 0.108 in the “V” band, in good agreement with the value of 0.118 reported by Morrison and Zellner (1979). Occultation and lightcurve data summarized by Mitchell et al. (1995) show this object as significantly elongated ( $a/b = 1.24$ ) which is consistent with that observed in Fig. 3 ( $a/b = 1.22$ ). Note that this asteroid appears significantly irregular in the reconstructions—it is definitely not a spheroid. No rotation is observed, as the two unsaturated images taken 6 min apart and the rotation period given by Lagerkvist et al. (1989) is 5.078 h.

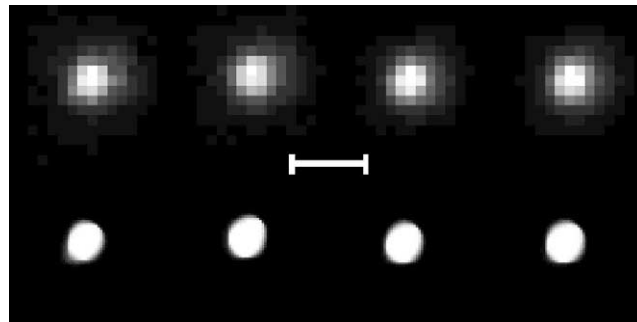


Fig. 4. Images of Asteroid 18 Melpomene before (top row) and after (bottom) reconstruction with the MISTRAL algorithm and a Tiny Tim PSF. Data taken on 18 January 1993 at 09:20 UT, 09:26 UT, 09:32 UT, and 09:38 UT, in the F439W filter. The line of sight is about  $50^\circ$  from the rotational axis. The scale bar is 0.37 arcsec long and celestial North is  $140^\circ$  CCW from straight up.

#### 4.2. 18 Melpomene

Figure 4, for 18 Melpomene, is laid out in a manner similar to Fig. 3. This asteroid was observed with the line of sight about  $50^\circ$  from the rotational axis given in the PDSSBN, so little rotational variation is expected given the 18 min duration of the observations compared to the rotation period of 11.572 h given by Lagerkvist et al. (1989). No significant variation is apparent within or between the images. The albedo is 0.155 in the “B” band, slightly lower than the value of 0.222 reported by Tedesco (1989) but in good agreement with the value of 0.149 reported by Morrison and Zellner (1979), while the radius is larger by one to two standard deviations (see Table 3). This object appears significantly elongated in the reconstructed images, with one end much larger than the other—clearly not a spheroid.

#### 4.3. 19 Fortuna

Figure 5, for 19 Fortuna, is laid out in a manner similar to Fig. 3. This dark “G” type object is the most regular of the set, and has a low albedo of 0.028. This value is significantly lower than Morrison and Zellner (1979) value of 0.037. The observations were made about  $45^\circ$  from the rotational axis given in the PDSSBN, so little rotational variation is expected given the 6 min duration of the observations and the rotational period of 7.445 h given by Lagerkvist et al. (1989). The elongation reported here is less than the  $2\sigma$  level—19 Fortuna is the most regularly shaped object observed here.

#### 4.4. 216 Kleopatra

Figure 6, for 216 Kleopatra, is laid out in a manner similar to Fig. 3. These reconstructions were first reported by Storrs et al. (2001). Note that while some variability is apparent among the raw WF/PC images, it is only after reconstruction (at improved spatial resolution) that the elongation (the asteroid is  $238 \times 121$  km averaged over the two best reconstructions) and rotation of the asteroid becomes visible. The

Table 3  
Asteroid data

Asteroid	Size		Axis ratios		Albedos		
	Restored size	Other reported sizes	This work	PSDSSBN	This work	TRIAD <sup>a</sup>	PDSSBN
9 Metis	222 × 182 ± 12 km	174 km, <sup>b</sup> 203 km, <sup>c</sup> 210 × 170 km <sup>d</sup>	1.22	<i>a/b</i> : 1.3, <i>b/c</i> : 1.24	0.108 ± 0.006 (V)	0.118	
18 Melpomene	155 × 170 ± 10 km	141 km <sup>b</sup>	1.1		0.155 ± 0.010 (B)	0.149	0.223 ± 0.009
19 Fortuna	225 × 205 ± 12 km	221 km <sup>c</sup>	1.1	<i>a/b</i> : 1.24, <i>b/c</i> : 1	0.028 ± 0.001 (V)	0.037	
216 Kleopatra	238 × 121 ± 19 km <sup>i</sup>	140 km, <sup>b</sup> 217 × 94 × 81 km, <sup>e</sup> 273 × 65 km <sup>f</sup>	1.97	<i>a/b</i> : 2.6, <i>b/c</i> : 1.3, 4.2, 6.0 <sup>f</sup>	0.077 ± 0.005 (B), 0.059 ± 0.003 (V)		0.116 ± 0.004
624 Hektor	363 × 207 ± 42 km <sup>i</sup>	370 × 211 km, <sup>g</sup> 423 × 232 × 175 <sup>h</sup>	1.75	<i>a/b</i> : 2.6, <i>b/c</i> : 1.3, 2.21 <sup>g</sup>	0.029 ± 0.001 (B), 0.023 ± 0.001 (V)	0.025	

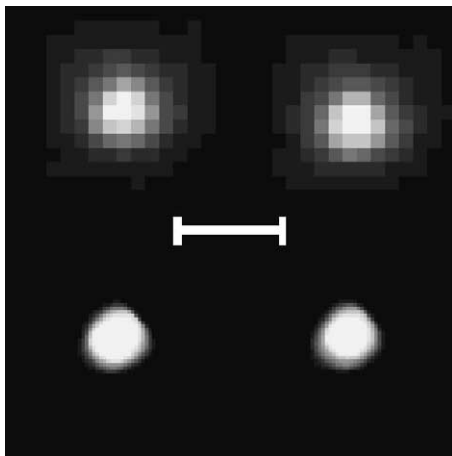
<sup>a</sup> From the TRIAD file (Morrison and Zellner, 1979).<sup>b</sup> From Tedesco (1989).<sup>c</sup> From Ostro et al. (1985).<sup>d</sup> From Mitchell et al. (1995).<sup>e</sup> From Ostro et al. (2000).<sup>f</sup> From Tanga et al. (2001).<sup>g</sup> From Tanga et al. (2002).<sup>h</sup> From Hestroffer et al. (2002).<sup>i</sup> Average of two highest SNR images, in F555W filter.

Fig. 5. Images of Asteroid 19 Fortuna before (top row) and after (bottom) reconstruction with the MISTRAL algorithm and a Tiny Tim PSF. Data taken on 10 September 1993 at 12:44 UT and 12:50 UT, in the F555W filter. The line of sight is about 40° from the rotational axis. The scale bar is 0.37 arcsec long and celestial North is 105° CCW from straight up. Note that the third image mentioned in Table 2 is saturated and is not included in the figure.

line of sight for these observations is only about 10° from the pole position reported in the PDSSBN, allowing observation of the rotation of the asteroid during the 18 min exposure sequence. This rotation rate matches that of 5.385 h reported by Lagerkvist et al. (1989).

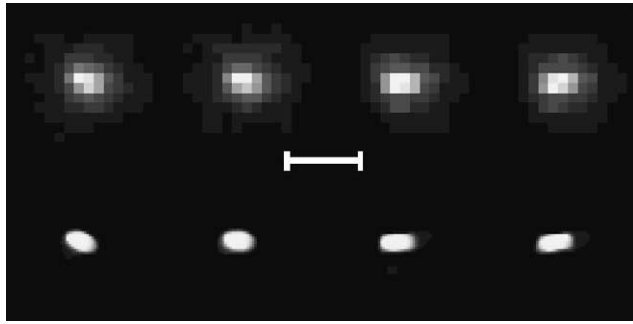
The observed dimensions are one standard deviation above those reported by the radar observations of Ostro et al. (2000). The resolution of the HST images is not good enough to resolve the central constriction reported by Ostro et al. (2000) or a possible gap discussed by Tanga et al. (2001) and Hestroffer et al. (2002a) (see above). Our lower limit to the axis ratio of 216 Kleopatra is smaller than that

reported by radar and AO observers. This is probably due to the limited phase coverage of the HST observations—our single epoch appears to coincide with a minimum in projected area (see Fig. 6b).

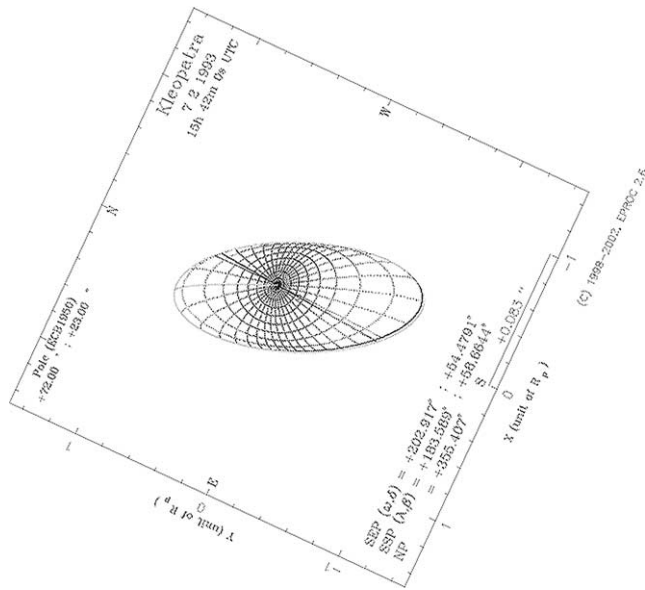
The albedo of 0.077 in the “B” band and 0.059 in the “V” band is markedly lower than the value of 0.116 reported in the PDSSBN (see Table 3). The blue color (B/V albedo ratio = 1.30) is unusual as other observers report this asteroid as being slightly red (B/V albedo ratio = 0.9–0.95). The 40% difference in color between the HST observations of 216 Kleopatra and those of other observers is significant at the four sigma level, much greater than the possible one sigma systematic in color discussed above. Possibly the polar region (observed here, see Fig. 6b.) is dominated by bluer material than that found on the more commonly observed equatorial regions. Note that no surface variegation is seen in the ratio images in Fig. 8, however.

#### 4.5. 624 Hektor

Figure 7, for 624 Hektor, is laid out in a manner similar to Fig. 3. No rotation is apparent, probably because the line of sight is about 45° from predicted pole positions in the PDSSBN and the short 20 min duration of the observations compared to the rotational period of 6.921 h reported by Lagerkvist et al. (1989). The image reconstructions are similar and show a slightly oblong body (the asteroid is 363 × 207 km averaged over the two best reconstructions) that is slightly larger than the values given by Storrs et al. (1999). The albedo is very low, as expected for a Trojan: 0.029 in the “B” band, and 0.023 in the “V” band. These values are in excellent agreement with that of 0.025 reported by Morrison and Zellner (1979), although again the blue color (B/V albedo ratio of 1.30) is significantly different (more



(a)

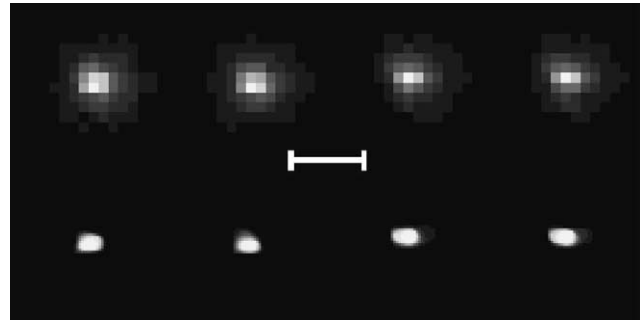


(b)

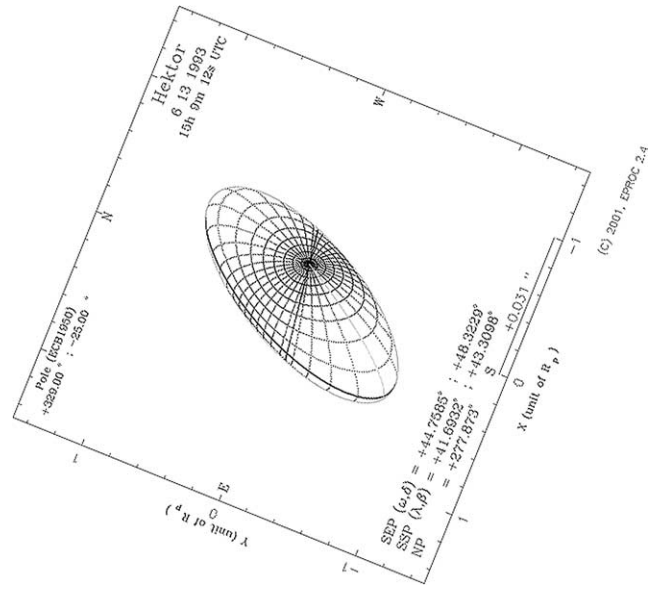
Fig. 6. (a) Images of Asteroid 216 Kleopatra before (top row) and after (bottom) reconstruction with the MISTRAL algorithm and a Tiny Tim PSF. Data taken on 2 July 1993 at 15:33 UT and 15:39 UT in the F439W filter, and at 15:45 UT and 15:51 UT in the F555W filter. Note the rotation of the asteroid during the observations—the line of sight is nearly aligned with the rotational axis. The scale bar is 0.37 arcsec long and celestial North is 70° CW from straight up. (b) Physical model of 216 Kleopatra at the time of observation, rotated to match the orientation of the HST images. From IMCCE, Obs. de Paris (Institut de Mécanique Céleste et Calcul d’Ephémérides) website ([http://www.imcce.fr/ephem/ephephys\\_eng/ephephys\\_fl.html](http://www.imcce.fr/ephem/ephephys_eng/ephephys_fl.html)). The restored HST images appear quite similar to the model calculated using the new rotational pole determined by Hestroffer et al. (2002b). Thanks to J. Berthier for adding this pole solution to the program.

than four standard deviations, again much greater than the possible  $1\sigma$  systematic in our process) from red colors measured elsewhere. The line of sight of the observations of 624 Hektor is about 40° from the rotational pole (see Fig. 7b.) reported in the PDSSBN. Thus light reflected from the polar regions doesn’t dominate the integrated light as much as for 216 Kleopatra, but still may contribute anomalously to the observed color.

Figure 8 shows the result of aligning and ratioing the “B” and “V” images of asteroids 216 Kleopatra (left) and 624 Hektor (right). The images were rotated to match the second



(a)



(b)

Fig. 7. (a) Images of Asteroid 624 Hektor before (top row) and after (bottom) reconstruction with the MISTRAL algorithm and a Tiny Tim PSF. Data taken on 13 June 1993 at 13:54 UT and 14:01 UT in the F439W filter, and at 14:08 UT and 14:14 UT in the F555W filter. The line of sight is nearly 40° from the rotational axis. The scale bar is 0.37 arcsec long and celestial North is 122° CCW from straight up. (b) Physical model of 624 Hektor at the time of observation (see Fig. 6). The restored HST images do not appear as elongated and are about 20° rotation ahead of the model.



Fig. 8. Color (B–V) maps of 216 Kleopatra (left) and 624 Hektor (right). Note that the images of 216 Kleopatra were rotated to match the first image of the series, before the map was made. No significant color variation is seen across the disks of the asteroids. Bright pixels at the edge of the images are due to slight misalignment of the original images.

image of each sequence. Color variation is not significant in these images—no surface features are observed.

## 5. Conclusions

We confirm the observation of Storrs et al. (1999) that no companions brighter than 5 magnitudes fainter than the parent asteroid are visible near these bodies. We report shapes, albedos, and sizes for these asteroids as given in Table 3. Each asteroid is the same size or slightly larger than reported in the literature (Morrison and Zellner, 1979; Tedesco, 1989), while the albedos are similar or slightly lower. For (216) Kleopatra and (624) Hektor, we have observations in more than one filter and these objects appear significantly ( $4\sigma$ ) more blue than observed from the ground. Our observations may be dominated by light from the polar regions of these bodies (see Figs. 6b and 7b).

The brightness enhancement on each asteroid's sunward limb noted by Storrs et al. (1999) appears to be an edge effect induced by the Maximum Entropy (MEM) image restoration. The MISTRAL algorithm used here gives a much more reliable restoration, and shows that while most of these bodies have a tendency to brighten slightly toward the sunward limb this modest effect is expected for a rough spheroidal surface.

No surface variegation was seen on any asteroid in the hemisphere observed (Figs. 3–7), and there are no color changes across the disk of the two objects observed in more than one filter (Fig. 8).

## Acknowledgments

The Hubble Space Telescope is operated by NASA and ESA. We acknowledge the support of NASA Contract NAS5-26555. We also thank the STScI amateur observing program, which sponsored program 4764. The NASA Planetary Data System Small Bodies Node (PDSSBN) provided an invaluable summary of diverse data. B.P.W. was supported by the NASA Exobiology Program. Two anonymous referees provided considerable help and insight.

## References

Close, L.M., 2000. A review of published Galactic and Solar System science: a bright future for adaptive optics science. In: Wizinowich, P.L. (Ed.), *Adaptive Optical Systems Technology*. In: Proc. SPIE, vol. 4007. SPIE, Bellingham, pp. 758–772.

Collins, N., Bohlín, R., 1997. STIS first-order low-resolution mode point-source sensitivity curves. In: Casertano, S., et al. (Eds.), 1997 HST Calibration Workshop. Space Telescope Science Institute, Baltimore.

Conan, J.-M., Mugnier, L.M., Fusco, T., Michau, V., Rousset, G., 1998. Myopic deconvolution of adaptive optics images using object and point spread function power spectra. *Appl. Optics* 37, 4614–4622.

Conan, J.-M., Fusco, T., Mugnier, L.M., Marchis, F., Roddier, C., Roddier, F., 2000. Deconvolution of adaptive optics images: from theory to practice. In: Wizinowich, P. (Ed.), *Adaptive Optical System Technology*. In: Proc. SPIE, vol. 4007. SPIE, Bellingham, pp. 913–924.

Hartmann, W.K., 1979. Diverse puzzling asteroids and a possible unified explanation. In: Gehrels, T. (Ed.), *Asteroids*. Univ. of Arizona Press, Tucson, pp. 466–479.

Hestroffer, D., Descamps, P., Kaasalainen, M., Tanga, P., Torppa, J., Berthier, J., Cellino, A., Lattanzi, M., Di Martino, M., Piironen, J., Zappala, V., 2002a. Comparison of topographic models for asteroids to the HST/FGS data. In: Proc. of Asteroids, Comets, Meteors (ACM 2002). In: ESA SP, vol. 500, pp. 493–496.

Hestroffer, D., Marchis, F., Fusco, T., Berthier, J., 2002b. Adaptive optics observations of Asteroid (216) Kleopatra. *Astron. Astrophys.* 394, 339–343.

Krist, J., 1993. *The Tiny Tim User's Manual*. Space Telescope Science Institute, Baltimore.

Lagerkvist, C.-I., Harris, A.W., Zappala, V., 1989. Asteroid lightcurve parameters. In: Binzel, R.P., Gehrels, T., Matthews, M.S. (Eds.), *Asteroids II*. Univ. of Arizona Press, Tucson, pp. 1162–1170.

Merline, W.J., Weidenschilling, S.J., Durda, D.D., Margot, J.-L., Pravec, P., Storrs, A.D., 2001. Asteroids do have satellites. In: Binzel, R.P., Bottke, W., Cellino, A., Paolicchi, P. (Eds.), *Asteroids III*. Univ. of Arizona Press, Tucson, pp. 289–312.

Mitchell, D.L., Ostro, S.J., Rosema, K.D., Hudson, R.S., Campbell, D.B., Chandler, J.F., Shapiro, I.I., 1995. Radar observations of Asteroids 7 Iris, 9 Metis, 12 Victoria, 216 Kleopatra, and 654 Zelinda. *Icarus* 118, 105–131.

Morrison, D., Zellner, B., 1979. Polarimetry and radiometry of the asteroids. In: Gehrels, T. (Ed.), *Asteroids*. Univ. of Arizona Press, Tucson, pp. 1090–1097.

Mugnier, L.M., Fusco, T., Conan, J.-M. 2003. MISTRAL: a myopic edge-preserving image restoration method: application to astronomical adaptive optics corrected long-exposure images. *JOSA A*. Submitted for publication.

Ostro, S.J., Campbell, D.B., Shapiro, I.I., 1985. Main-belt asteroids: dual-polarization radar observations. *Science* 229, 442–446.

Ostro, S.J., Hudson, R.S., Nolan, M.C., Margot, J.-L., Scheeres, D.J., Campbell, D.B., 2000. Radar observations of Asteroid 216 Kleopatra. *Science* 288, 836–839.

Saint-Pé, O., Combes, M., Rigaut, F., 1993. Ceres surface properties by high-resolution imaging from Earth. *Icarus* 105, 271–281.

Storrs, A., Weiss, B., Zellner, B., Burleson, W., Sichiuti, R., Wells, E., Kowal, C., Tholen, D., 1999. Imaging observations of asteroids with Hubble space telescope. *Icarus* 137, 260–268.

Storrs, A.D., Dunne, C., Conan, J.-M., Mugnier, L., 2001. HST imaging observations of Asteroid 216 Kleopatra. *Bull. Am. Astron. Soc.* 32, 1487. Abstract.

Tanga, P., Hestroffer, D., Berthier, J., Cellino, A., Lattanzi, M.G., Di Martino, M., Zappala, V., 2001. HST/FGS observations of the Asteroid (216) Kleopatra. *Icarus* 153, 451–454.

Tanga, P., Hestroffer, D., Cellino, A., Lattanzi, M.G., Di Martino, M., Zappala, V., 2002. Shape and size measurements of asteroids by the HST Fine Guidance Sensors. In: Proc. of Asteroids, Comets, Meteors (ACM 2002). In: ESA SP, vol. 500, pp. 517–520.

Tedesco, E.F., 1989. Asteroid magnitudes, UVB colors, and IRAS albedos and diameters. In: Binzel, R.P., Gehrels, T., Matthews, M.S. (Eds.), *Asteroids II*. Univ. of Arizona Press, Tucson, pp. 1090–1138.

Tedesco, E.F., Noah, P.V., Noah, M., Price, S.D., 2002. The supplemental IRAS minor planet survey. *Astrophys. J.* 123, 1056–1085.

Zellner, B.H., Albrecht, R., Binzel, R.P., Gaffey, M.J., Thomas, P.C., Storrs, A.D., Wells, E.N., 1997. Hubble Space Telescope images of Asteroid 4 Vesta in 1994. *Icarus* 128, 83–87.